# Multiphase aluminum equations of state via density functional theory

Travis Sjostrom, Scott Crockett, and Sven Rudin
*Theoretical Division, Los Alamos National Laboratory, Los Alamos, New Mexico 87545, USA*
(Received 7 April 2016; revised manuscript received 5 July 2016; published 3 October 2016)

We have performed density functional theory (DFT) based calculations for aluminum in extreme conditions of both pressure and temperature, up to five times compressed ambient density, and over 1 000 000 K in temperature. In order to cover such a domain, DFT methods including phonon calculations, quantum molecular dynamics, and orbital-free DFT are employed. The results are then used to construct a SESAME equation of state for the aluminum 1100 alloy, encompassing the fcc, hcp, and bcc solid phases as well as the liquid regime. We provide extensive comparison with experiment, and based on this we also provide a slightly modified equation of state for the aluminum 6061 alloy.

DOI: 10.1103/PhysRevB.94.144101

## I. INTRODUCTION

The importance of aluminum as a material subject of scientific investigation as well as an essential and ubiquitous material of application of all sorts cannot be overstated. As such a thorough understanding of aluminum's thermodynamic properties is of primary interest and has been explored through numerous experimental and theoretical studies. In particular experimental approaches continue to press into the regime of extreme conditions of pressure and temperature, where aluminum is both examined to generate fundamental results and used as a standard [1–3]. Yet experimental results in the so-called warm dense matter (WDM) regime, which can be roughly characterized as having densities ranging from ambient solid density to several times compression and with temperature from a few thousand to a few million Kelvin, do continue to be difficult to obtain and sparse. Equally, theoretic approaches for WDM suffer from the difficulties of describing fluids composed of moderately to strongly coupled partially ionized ions and quantum degenerate electrons [4].

In this paper we examine the thermodynamic properties of aluminum through density functional theory (DFT) based methods. This includes calculation of the cold curve and the pressure induced phase transitions along it. Through analysis of the phonon spectrum the response of the solid phases to temperature is examined. For the liquid and WDM regime we perform quantum molecular dynamics (QMD) simulations incorporating both orbital-based (Kohn-Sham) and orbital-free DFT. This combination of methods allows us to accurately characterize aluminum from melt to the ideal gas limit. Finally, these results are used, in conjunction with the best available experimental data, to generate new tabular multiphase equations of state (EOS) for the nearly pure aluminum 1100 alloy and the aluminum 6061 alloy which is commonly used in shock experiments. The 6061 alloy is less dense than aluminum 1100 and demonstrates a slightly stronger shock response [5]. While previous EOS for aluminum have been constructed [6–8], none provide the high pressure solid phases, or have had access to the broad range of high accuracy simulations we have performed to constrain particularly the liquid state. However, several recent EOS have been constructed for different materials which are both multiphase and inclusive of the warm dense matter regime and have also highly relied on simulation data [9–11].

## II. DFT CALCULATIONS

### A. Crystal phases: Cold curve and phonons

Calculations in orbital-based (Kohn-Sham) DFT were performed using the VASP plane wave code [12], utilizing the Perdew-Burke-Ernzerhof (PBE) [13] exchange-correlation functional and a PAW pseudopotential [14] with three electrons in the valence space. We also compared local density approximation (LDA) exchange-correlation calculations for the cold curve and found better agreement with the known zero temperature density using PBE [15]. Total energy calculations employ a plane wave cutoff energy of 300 eV, a **k**-point mesh of density 60 $\text{Å}^{-1}$, and the linear tetrahedron method with Blöchl corrections [16]; the self-consistent cycles are converged to 1 $\mu$eV. Force calculations rely on the same parameters with the exception of converging the self-consistent cycles to 0.01 $\mu$eV. The molecular dynamics (MD) simulations employ a $4 \times 4 \times 4$ **k**-point mesh, Fermi-Dirac smearing with a 0.1 eV energy scale, convergence of the self-consistent cycles to 10 $\mu$eV, and a time step of 5 fs.

We have calculated using Kohn-Sham DFT the cold curves of close-packed fcc, hcp, bcc, and dhcp phases of aluminum. At zero temperature fcc is the ground state up to a pressure of 176 GPa, where Al transitions to the hcp phase, and then at a pressure of 373 GPa Al transitions to the bcc phase. These results are consistent with earlier DFT calculations [17,18]. Table I lists the calculated parameters of the cold curves, i.e., the equilibrium density $\rho$, the bulk modulus, $B$, and its pressure derivative $B'$, along with the Debye temperature $\theta_D$ (evaluated from the phonon spectra described below).

In order to include thermal effects, we have performed calculations of the phonon spectra. Figure 1 compares for fcc Al the experimental data with the results obtained from two methods, the direct force method [19] and by extracting the frequencies from MD simulations. Both methods rely on supercells consisting of $4 \times 4 \times 4$ fcc unit cells of one and four ions, respectively. The former involves displacing one ion and calculating the Hellman-Feynman forces on all ions, from which the force constants are evaluated and used to find the phonon frequencies in the quasiharmonic approximation. The latter relies on constant-energy MD simulations; the atomic positions are used to evaluate the dynamic structure factor for wave vectors commensurate with the supercell, and the results are then fit to Gaussians to find the frequencies reported in Fig. 1.

 

TABLE I. Parameters from the DFT calculations for aluminum

| | $\rho$ (g/cm$^3$) | $B$ (GPa) | $B'$ | $\theta_D$ (K) |
|---|---|---|---|---|
| fcc | 2.711 | 81 | 4.13 | 385 |
| hcp | 2.686 | 76 | 4.14 | 367 |
| bcc | 2.645 | 71 | 4.12 | 355 |

The phonon spectra were then used to evaluate the free energies of the system for each crystal structure at a sequence of volumes for a series of temperatures. This allowed us to map out the phase boundaries by calculating the Gibbs free energy. Here we found good agreement with the all-electron calculations of Kudasov *et al.* [21]. One key feature of interest is that the hcp phase does not extend to melt and there is an fcc-hcp-bcc triple point at about 255 GPa and 2900 K.

### B. Liquid phase: QMD

Kohn-Sham based QMD simulations have become the gold standard for calculations of warm dense matter. The success lies in the accurate treatment of the quantum nature of the electrons, through the Mermin-Kohn-Sham DFT [22], and the ionic, possibly strongly coupled, fluid motion, through the molecular dynamics of the classically treated ions. Yet this approach suffers a prohibitive scaling issue with increasing temperature due to the increasing number of Kohn-Sham orbitals that must be calculated to obtain the electron density. An alternative approach, without such an issue, is provided by orbital-free DFT where the electron density is found through direct minimization of the total free energy. The issue here, however, is the accuracy of the necessary approximation for the kinetic (plus entropic) free energy functional, $F_s[n]$. While the simple Thomas-Fermi approximation has been used successfully at very high temperatures, there is significant loss of accuracy at lower temperatures [23]. Recently we have developed and applied an approach correcting the Thomas-Fermi approximation, $F_{\rm TF}$, through an additional density gradient term in which the leading coefficient $\lambda$ is determined by matching Kohn-Sham calculations of the pressure at lower temperatures of 5–10 eV [24],

$$F_s[n] = F_{\rm TF}[n,T] + \lambda \int \frac{|\nabla n(\mathbf{r})|^2}{8n(\mathbf{r})} d\mathbf{r} \,. \tag{1}$$

This then allows for extension through very high temperatures. It is this approach we use in this work, for which the development and implementation details may be found in Ref. [24]. However, unlike in that work, here we found the coefficient of the gradient term to be negligibly small, and so we have effectively performed for aluminum Kohn-Sham calculations up to temperature of 6 eV and Thomas-Fermi calculations above that. The overlap of the Kohn-Sham and orbital-free calculations can be seen along several isochores in Fig. 2; here the differences are less than 2% in the pressure, while one can see errors of 30% or more when using Thomas-Fermi at lower temperatures [25].

In the Kohn-Sham QMD we have used the plane wave code Quantum-Espresso [26] to perform calculations with periodic unit cells of 60 atoms. We employed the PBE exchange-correlation functional and three-electron PAW pseudopotentials [27] as in the crystal case (albeit using a different code). For the temperatures and densities ranges we calculated, it was sufficient to perform gamma point calculations. For densities above 8.5 g/cm$^3$ and temperatures at 6 eV and above we used an 11-electron norm conserving pseudopotential [17], which enabled extension to densities of 13.5 g/cm$^3$. The plane wave energy cutoffs were 30 Ry (1 Ry = 13.605 eV) for the three-electron PAW and 100 Ry for the 11-electron norm conserving pseudopotential.

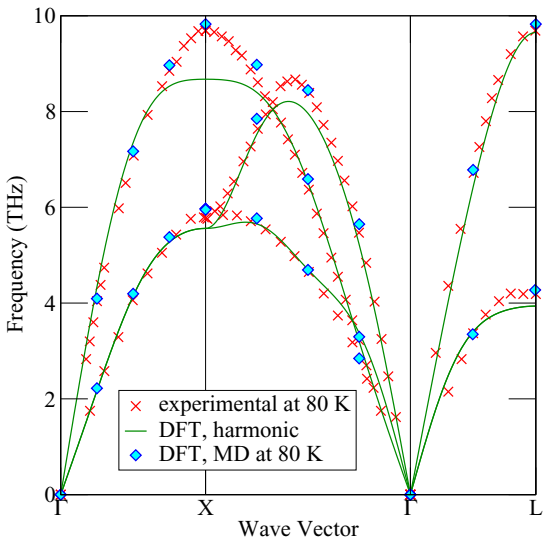


FIG. 1. Phonon spectrum of fcc aluminum at the experimental density. Experimental data stems from Stedman and Nilsson [20]. Phonons calculated in the quasiharmonic approximation show overall good agreement with experiment; discrepancies are not due to shortcomings in the DFT itself but arise from temperature effects. These effects are included in the frequencies extracted from molecular dynamics (MD) simulations, which show excellent agreement with experiment.

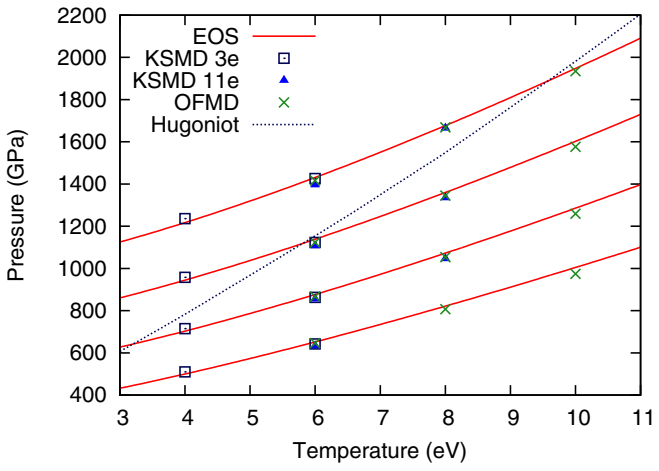


FIG. 2. Pressure isochores for liquid Al showing the transition for Kohn-Sham to orbital-free calculations. The densities are 8.5, 7.5, 6.5, and 5.5 g/cm$^3$. The principle Hugoniot from the EOS is shown as well for reference.

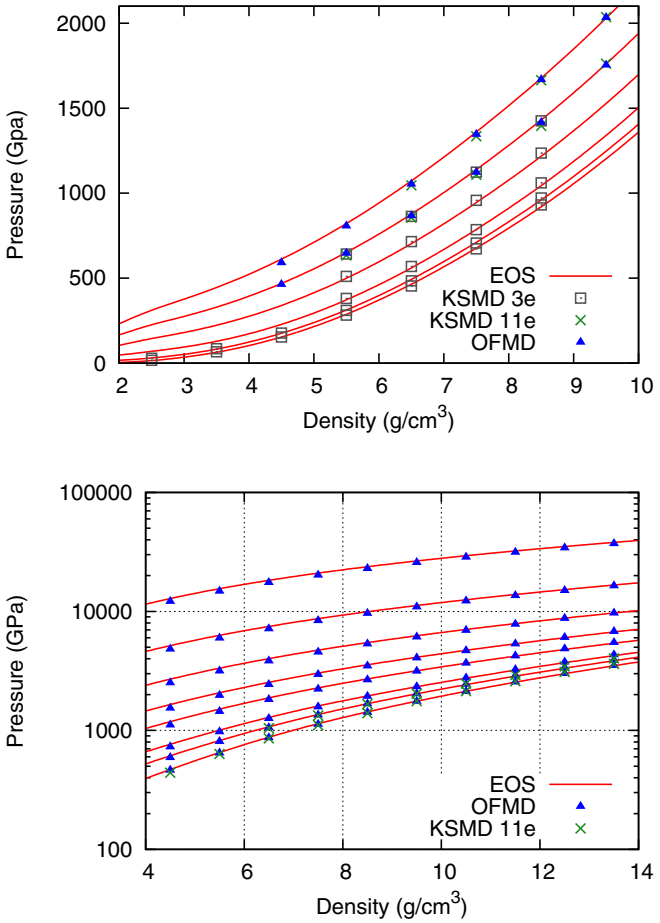


FIG. 3. Pressure isotherms for liquid Al with temperatures of 8, 6, 4, 2, 0.86, 0.39 eV (upper panel) and 100, 50, 30, 20, 15, 10, 8, 6 eV (lower panel).

In the orbital-free calculations we used 72 atoms and the density was optimized on a $64^3$ grid. We used LDA exchange correlation for convenience in the orbital-free calculations, as the difference between PBE and LDA results are negligible with respect to the uncertainty arising from the orbital-free kinetic approximation, particularly at the elevated temperatures above 6 eV. Additionally we used a local pseudopotential based on average-atom Thomas-Fermi calculations [23], with a cutoff radius $r_c = 0.6 r_{\mathrm{WS}}$, where $r_{\mathrm{WS}}$ is the Wigner-Seitz radius.

The results are shown in Fig. 3. In the upper panel the lower temperature Kohn-Sham results (KSMD) are shown as well as the overlapping calculations of the orbital-free molecular dynamics (OFMD). In the lower panel the extension to high temperature is shown, along with the agreement of the Kohn-Sham results at low temperature. Additionally the solid curves show the results of our EOS, which will be described below.

## III. MULTIPHASE EOS

### A. Construction

The overall EOS consists of the liquid phase as well as the ambient solid fcc phase and the higher pressure crystal phases hcp and bcc. We constructed each of the four phases separately and then determined the phase boundaries by consideration of the Gibbs free energy [28]. For each phase we used the standard, but nonunique, decomposition of the total Helmholtz free energy into the three terms,

$$F = F_0(\rho) + F_i(\rho,T) + F_e(\rho,T), \tag{2}$$

where $F_0$ is the zero temperature energy curve, and $F_i$ and $F_e$ are the thermal contributions of the ions and electrons, respectively. Each component utilizes various models. The calculated DFT cold curves, and phonon derived Debye temperatures (this is all we are using the phonons for) are inputs for the EOS. We can also derive other model parameters, such as the Grüneisen parameter from our grid of KSMD calculations for the liquid. With a candidate EOS, we can compare the pressures from the EOS with those from QMD results, as well as compare constraining experimental, and other theoretical data, which then allows us to refine the parametrization of our models.

First, we consider the liquid phase. Here, we used the model of Johnson [29] to ascertain $F_i$ from near melt, where ion coupling is very strong, completely through the ideal gas limit at very high temperature. The QMD data is essential to determine then both $F_0$ and to fix the parameters of the ion model such that the transition to the ideal limit is physically correct. Additionally, for $F_e$ we use the Thomas-Fermi-Dirac average atom model. This electron model is used for all phases though it is only a significant contribution in the liquid phase. As shown in Fig. 3 very good agreement is found between the EOS and the QMD results.

In all of the solid phases we used a Debye model for $F_i$. Here the DFT calculated cold curves, from Sec. II A, are used to determine $F_0$, while the phonon calculations determine the Debye temperatures. This provides the solid-solid phases transitions both along the cold curve and at finite temperature. One caveat is that the DFT results are subject to error in the

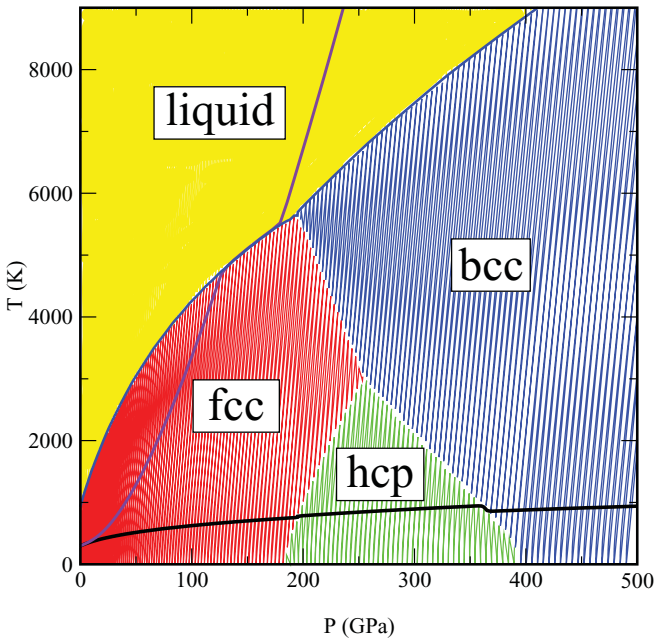


FIG. 4. Phase diagram for aluminum. The solid curves are the principle hugoniot, melt curve, and principle isentrope, from top to bottom.

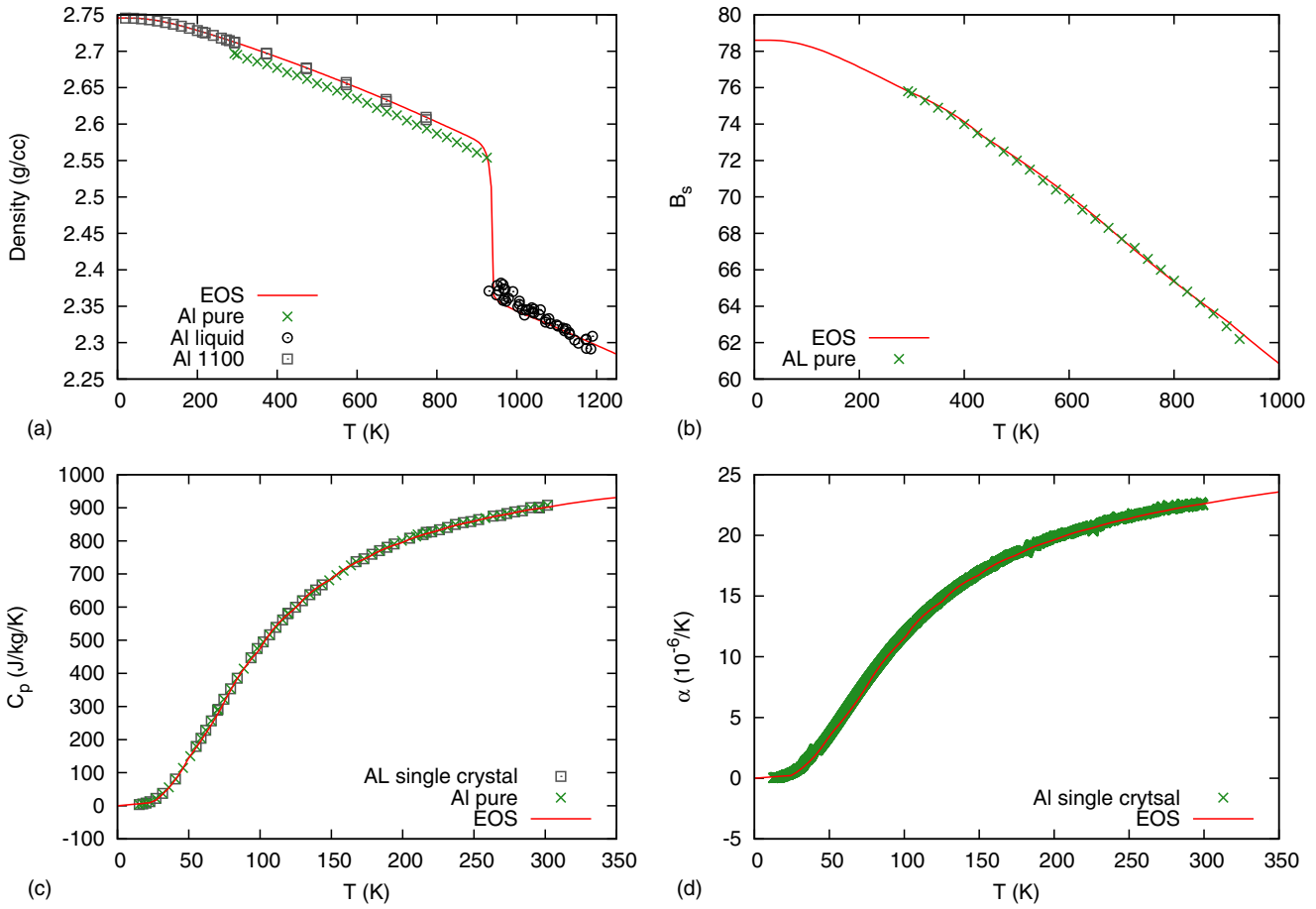


FIG. 5. Ambient pressure thermal expansion (a) in solid and liquid phase. The EOS agrees with the aluminum 1100 [31,32] and the liquid data [33–38]. For comparison the pure aluminum [39] fcc phase thermal expansion is shown. Experimentally determined derivative properties of the bulk modulus [39] (b), specific heat [40,41] (c) and the linear expansion coefficient [42] (d) show good agreement with the EOS.

exchange-correlation approximation that is not negligible at low temperature. For example, our DFT (PBE) equilibrium density is 2.711 g/cm$^3$ whereas the experimentally determined value is 2.734 g/cm$^3$ [15]. Thus our EOS cold curve is shifted some from the DFT results for the fcc phase to agree with the experimental data, as will be shown in the next section. In the other solid phases where no such experimental data is available we have assumed this shift to be global. Further details of the EOS models are given in the Appendix.

### B. Results

To begin we consider, in Fig. 4, the overall phase diagram to 500 GPa and to temperatures well above melt. This encompasses the DFT predicted zero temperature phases transitions of fcc→hcp at 176 GPa and hcp→bcc at 373 GPa. Additionally the Debye temperature calculated from the DFT based phonon analysis, along with the Grüneisen parameter determined from the thermal expansion data of the fcc phase, fix the phase boundaries including the fcc-bcc-liquid triple point at 195 GPa and 5650 K, and the fcc-hcp-bcc triple point at 255 GPa and 2900 K. It has been shown elsewhere that the bcc phase is stable up to 3.2 TPa [30]. Also shown on the plot for reference are the principle hugoniot, the melt curve, and the principle isentrope.

Next, with some finer analysis we examine the ambient isobaric properties of aluminum. In Fig. 5(a) we show the thermal expansion from the EOS compared to the available experimental results for the aluminum 1100 solid and liquid aluminum. Additionally the expansion of pure aluminum is shown, which illustrates that the essential difference in the expansion is a shift in the density of 0.1 g/cm$^3$ from 2.712 for aluminum 1100 to 2.70 for pure aluminum at 298 K. This then suggests that for some derivative properties, such as the expansion coefficient, that benchmarking of the aluminum 1100 EOS to the available experimental data of pure aluminum is valid. Figures 5(b)–5(d) shows the bulk modulus $B_S$, the specific heat capacity $C_p$, and the linear thermal expansion coefficient $\alpha$ for the fcc phase at 1 atm pressure. The EOS is in very good agreement with the experimental data which is for both single crystal aluminum and otherwise pure aluminum. It is of note that these EOS results are highly dependent on the Debye temperature, for which we haven taken the value of 385 K directly from the DFT calculation. Given the good agreement then we are confident in using the DFT derived Debye temperatures for the the higher pressure hcp and bcc phases as well.

Next we consider the shock compression and high pressure melting. Figure 6 shows the shock Hugoniot experimental data for aluminum 1100 with our EOS. In Fig. 6(a) it is of note

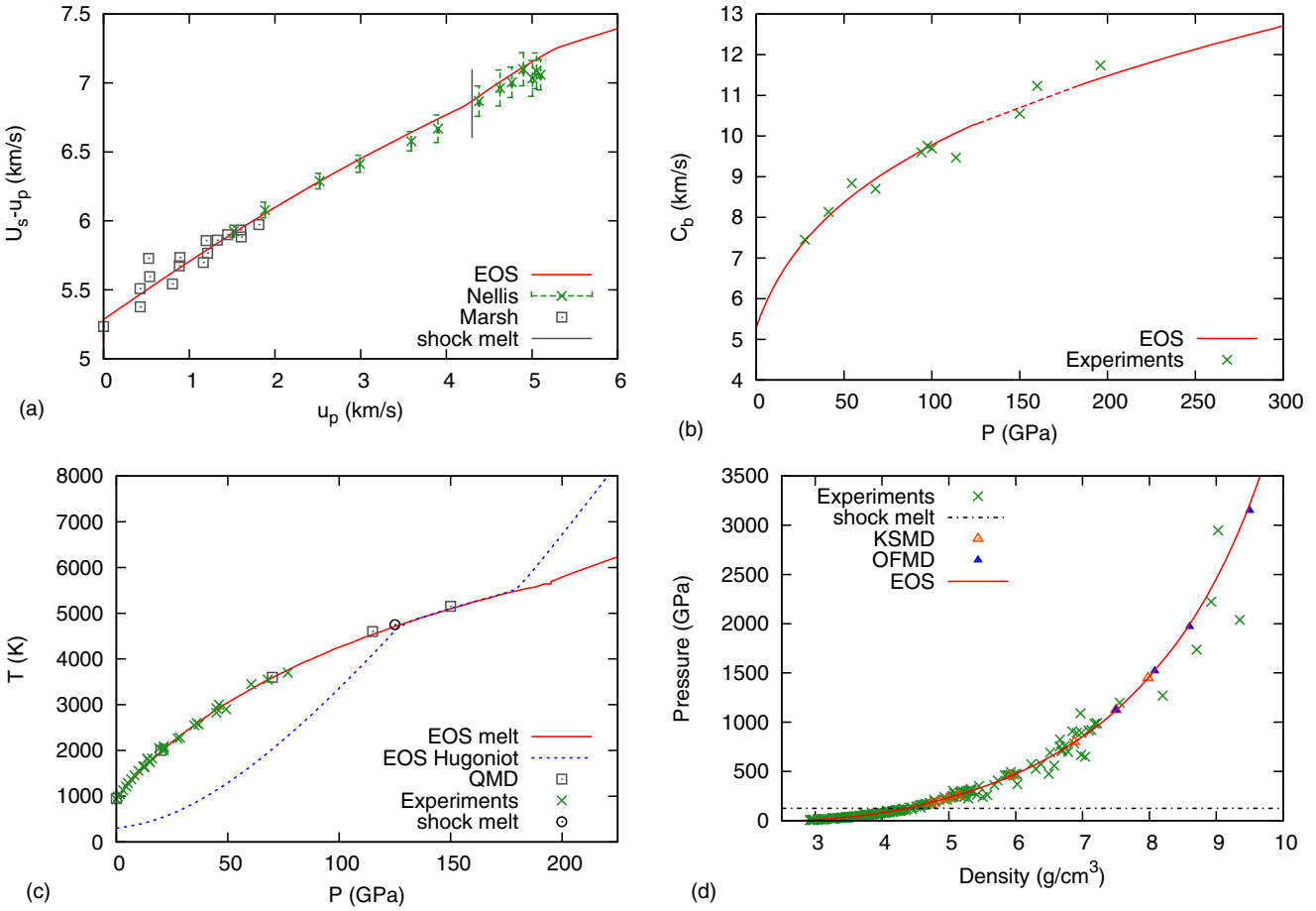


FIG. 6. EOS comparisons with shock data: (a) Shock Hugoniot velocity data for aluminum 1100 [5,43]; (b) sound velocity along the aluminum 1100 Hugoniot [44–46]; (c) melt curve data [47,48] for pure aluminum, including QMD based results [49]; (d) high pressure shock data [43,54–75] along with our KSMD and OFMD results.

that we plot $U_s - u_p$ on the $y$ axis for further clarity than the standard $U_s$ vs $u_p$ plot [50], where $U_s$ is the shock velocity and $u_p$ the particle velocity. We have marked the shock melt which is at $u_p = 4.3$ km/s and one can see the complete transition to the liquid phase by the change in slope at $u_p = 5.3$ km/s. In Fig. 6(b) we have plotted the sound velocity $C_b$, along the Hugoniot, where the dotted line represents the melting region with the fcc phase given by the solid curve to the left and the liquid phase given by the solid curve to the right. Then in Fig. 6(c) the temperature along the Hugoniot is shown together with the melt curve. The melt curve is seen to be in very good agreement with both *ab initio* QMD results [49,51] and experimental results, including the shock melt at 125 GPa and 4700 K [52]. The entropy increase at melt and ambient pressure is slightly higher at 1.68 $k_B$/atom compared with the calculated value of about 1.38 [53].

Extending now to shock compressions significantly above the shock melt, we consider various experiments of nearly pure aluminum. Those experiments are compared with the Hugoniot calculated from the EOS in Fig. 6(d). Additionally we show the points calculated along the Hugoniot directly from our QMD simulations, which are in agreement with previous all-electron [76] and pseudopotential [77] calculations. These points are determined by the Rankine-Hugoniot jump conditions

$$E_f - E_i = (P_f + P_i)(V_i - V_f)/2 \,, \tag{3}$$

$$(P_f - P_i) = \rho_i U_s u_p \,, \tag{4}$$

$$\rho_f = \rho_i U_s/(U_s - u_p) \,, \tag{5}$$

for the internal energy $E$, pressure $P$, and volume $V$ between the initial and final states. The conditions also connect the experimental shock $U_s$ and particle $u_p$ velocities with the thermodynamic states, which relates Fig. 6(a) to Fig. 6(d). For the initial state Kohn-Sham DFT is used to calculate the energy and pressure at the experimental initial density of 2.712 g/cm$^3$ and in the fcc phase. Then QMD is performed to find the temperature and density conditions with results that satisfy the jump conditions.

In transitioning from the orbital-based Kohn-Sham calculations to the orbital-free DFT calculations the change in pseudopotential used requires accounting for a shift in the zero of energy. There are two corrections involved so that we may compare energies directly between the orbital-free and Kohn-Sham results. First is the major correction between the Kohn-Sham PAW pseudopotential and the orbital-free pseudopotential. We have matched pressures at 6 eV, for a given density and temperature, and have then immediately the

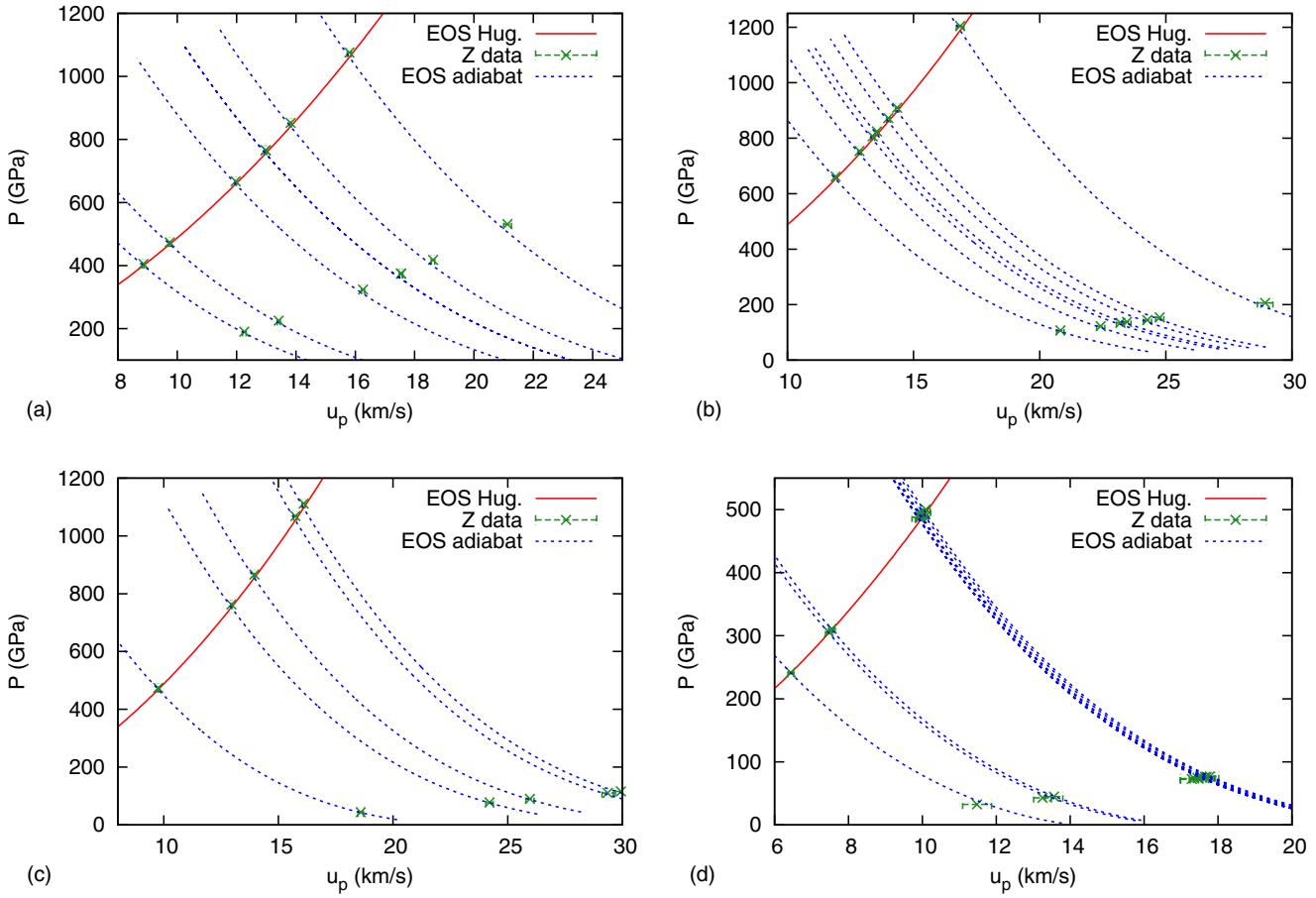


FIG. 7. Shock release data for 6061 aluminum [79,80]. Adiabats calculated from the EOS for the experimental release points show agreement within the experimental errors of the measured final states.

energy shift at that point given by the difference in energies. This is taken as the principle shift in energy for a given isochore. However, as we increase temperature the orbital-free pseudopotential does change, and so we perform additional snapshot calculations at given ion positions with both the 6 eV pseudopotential and the pseudopotential for the temperature we are actually at and compute the difference in energies which provides a much smaller secondary correction.

In the compressed region away from the Hugoniot we can compare with both double shock data as well as shock release data. In Fig. 7 we have plotted the shock and release data from the Z-machine experiments. The material used in the experiments is 6061 aluminum, and it is that specific EOS which is plotted here, however for calculations in this regime the difference between the 1100 and 6061 EOS are negligible. The experiments first determine the shocked state along the aluminum Hugoniot then through impedance matching the isentropic release point is determined by observing the shock continuing through a secondary standard material. In these experiments the impedance match materials are a plastic material, polymethylpentene (TPX) in Fig. 7(a), and silica aerogel of different densities, which provide a range from relatively shallow release [Fig. 7(a)] to a deep release [Figs. 7(c) and 7(d)]. Across all these results the EOS adiabats calculated from the shock release point are in very good agreement, that is within the approximate 1% experimental uncertainty, with the measured values. This shows our constraint of the EOS to the QMD simulations in the liquid regime yields high accuracy away from the Hugoniot.

The double shock data of Nellis for aluminum 1100 is shown in Fig. 8. Here the curves represent the principle shock Hugoniot (dotted) and reshock (dashed) from the pressures along the Hugoniot of 163, 102, and 65 GPa. The slope

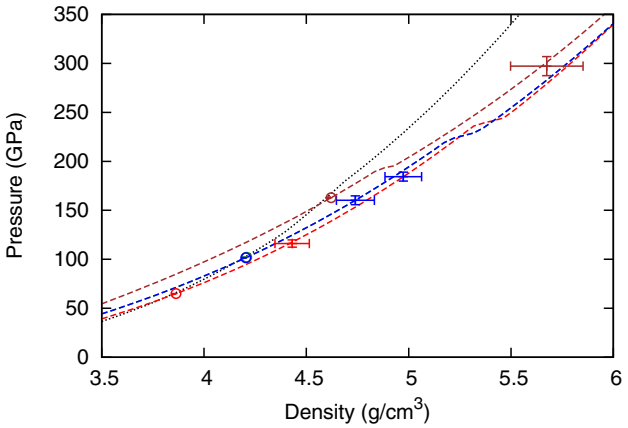


FIG. 8. Double shock data for aluminum 1100 [78] show agreement with EOS.

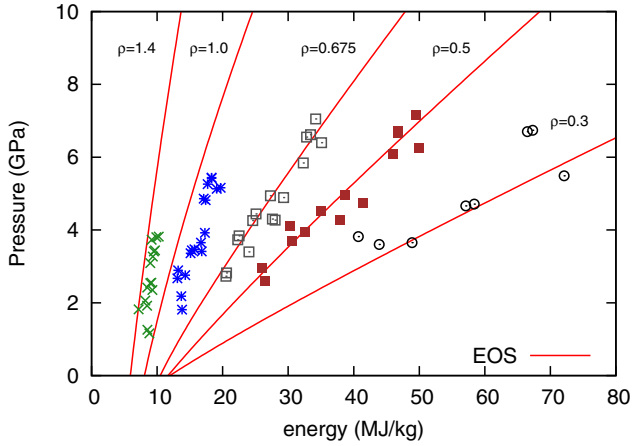


FIG. 9. Expanded fluid region experimental data [81] compared with the EOS results.

change occurring in the second shock marks the transition from fcc to bcc. In the highest pressure case, however, the initial shocked state is along the melt curve and the second shock curve follows the melt curve with the slope change, at about $u_p = 4.9$, marking the triple point.

In the expanded fluid region we make use of recent experiments performed on aluminum foils. The results are shown in Fig. 9 where pressure is plotted against the internal energy. At the highest densities the EOS shows higher pressure than the experiment for the given energies, but by no more than 0.5 GPa. This region near 1 g/cm$^3$ and above represents the transition region of the EOS cold curve from a Lennard-Jones model to a Rose-Vinet model. The agreement does become better with lower density, and this allows us to predict the value of the aluminum critical point [82] at a density of 0.375 g/cm$^3$ and a temperature of 8400 K, which is close to the value given in Ref. [83]. We find the value of the critical point by identifying the inflection point,

$$\left(\frac{\partial P}{\partial V}\right)_T = \left(\frac{\partial^2 P}{\partial V^2}\right)_T = 0\,, \tag{6}$$

through inspection of the EOS isotherms. Below the critical point the constructed EOS does develop van der Walls loops due to the Lennard-Jones model used in that region, and so we perform a Maxwell construction to remove them.

### C. 6061 aluminum

With the exception of Fig. 7 all the EOS results up to this point have been for 1100 aluminum. In fact, though, in that compressed liquid region there is no distinguishable difference between 1100 and 6061, and further for most of the results there is very little difference. In this section we highlight where there are some noticeable differences. Firstly, there is the change in ambient density of 2.712 to 2.70 g/cm$^3$. We note that this density change brings the thermal expansion for aluminum 6061 into agreement with the pure aluminum data shown in Fig. 5(a). Shown in the upper panel of Fig. 10 is the shock Hugoniot in terms of $U_s$ and $u_p$ which is a bit different than for 1100 aluminum. Of note is a difference in the $u_p = 0$ intercept which translates to a difference in the cold

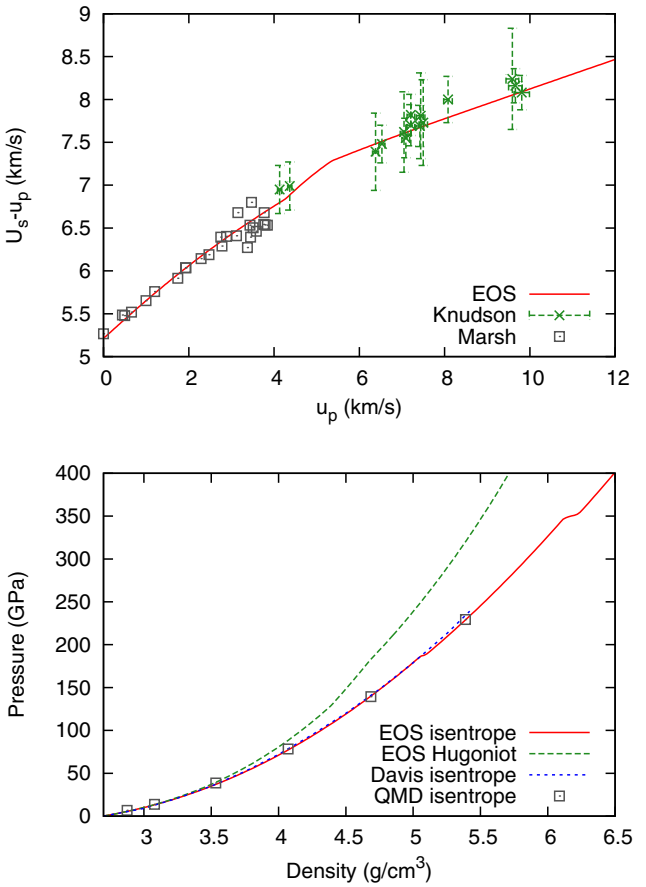


FIG. 10. Shock [5,74] and isentrope [84,85] results for 6061 aluminum.

curve bulk modulus of 78.5 GPa for 6061 and 81 GPa for 1100. In compensating fashion the bulk modulus pressure derivative is increased from 4.7 to 4.8 for fcc aluminum 6061. Other than those two changes to the fcc phase, the only change is a 0.012 g/cm$^3$ shift in the cold curve applied to all of the phases. In the lower panel is a comparison of the principle isentrope between the EOS, QMD calculations [84], and experimental data [85] for 6061. Excellent agreement is seen up to 5.1 g/cm$^3$ where the phase change from fcc to hcp occurs. Though no evidence of the phase change is seen in this experimentally derived isentrope, earlier experimental compression results suggest it [86], as do recent shock adiabat results [87]. By contrast, the aluminum 1100 isentrope and Hugoniot (which are not shown) lie at a slightly lower pressures by 1–2%, when evaluated from the same initial conditions.

## IV. CONCLUSION

We have performed density functional based calculations for aluminum. These calculations encompass the cold curve including the zero temperature pressure induced phase transitions from fcc to hcp at 176 GPa and from hcp to bcc at 373 GPa. Additionally we completed highly accurate phonon calculations based on equilibrium force calculations as well as low temperature QMD, from which values of the Debye temperature and the Grüneissen parameter for the individual solid phases have been extracted. Additionally QMD has been

performed in the liquid region from 0.4–100 eV, by employing both Kohn-Sham and orbital-free density functional theory. Here we extended the Kohn-Sham calculation to 8 eV and found overlap between the Kohn-Sham and Thomas-Fermi orbital-free calculations at 6 eV.

We then used our results to construct a multiphase aluminum EOS, specifically for aluminum alloys 1100 and 6061. Along with the DFT results, we made use of the most accurate and modern experimental data available for aluminum including for fcc phase and liquid regime, and for single crystal aluminum as well as for 1100 and 6061. While DFT is in general a highly accurate theoretical approach, some deficiencies do exist, such as in the lattice constant calculation of aluminum due to the exchange-correlation functional. Therefore we have used to the greatest extent possible the DFT results as constraint to the EOS construction, and then appealed to the experimental data, where it provides a clear correction, for adjustment of the EOS. We would suggest such an approach is completely natural when the goal is the most accurate EOS, and is most helpful here in the cases of the high pressure hpc and bcc phases for which nearly no experimental data is available, yet we may modify the EOS from the pure DFT results relative to the fcc modification to provide overall improvement. Future experiments, such as reshock and isentropic compression, may validate this by accurately identifying the conditions of the crystal phase transitions.

## ACKNOWLEDGMENTS

We would like to thank D.C. Wallace for helpful and encouraging discussions and J.C. Lashley for providing his aluminum crystal data. This work was performed under the auspices of Los Alamos National Laboratory, which is operated by Los Alamos National Security, LLC, for the National Nuclear Security Administration of the U.S. Department of Energy under Contract No. DE-AC52-06NA25396.

## APPENDIX

Here we provide further details of the EOS models and their parameters used to generate the multiphase tabular SESAME EOS. First we recall that for each of the aluminum phases the total free energy is given by a combination of the cold curve $F_0$ and thermal contributions of the ions $F_i$ and the electrons $F_e$.

As noted in the main text, the final contribution is from a Thomas-Fermi-Dirac average atom (AA) calculation [88], where the actual contribution $F_e$ is given by the difference between an AA calculation at a given density and temperature and an AA calculation at the same density and zero temperature. This must be tabulated at all density and temperature grid points of the EOS.

Next the cold curve $F_0$ is in all cases given at low density, up to the ambient solid density, by a Lennard-Jones model and at high density, above 3.5 times the ambient density, by the Thomas-Fermi-Dirac approximation. The matching at those densities is as prescribed in Ref. [89]. The modified Lennard-Jones model depends directly on two other parameters: the cohesive energy which was taken for solid phases at the experimental value of 78.1 kcal/mol [90], and slightly lower for the liquid phase at 70 kcal/mol, and an exponent in the functional form which is 0.7 for the solid phases and 0.65 for the liquid phase. In the interim the solid phases are given by a Rose-Vinet model with the bulk modulus and its derivative as given in Table II, with a slight increase of the equilibrium density from the DFT values to correct for the exchange-correlation approximation error (as mentioned in Sec. III A). Also $B'$ is increased to provide better agreement between the EOS and DFT curves at higher pressure than given by the equilibrium $B'$ of Table I. The liquid regime uses a Birch-Murnaghan expansion in $\eta = [(\rho/\rho_0)^{2/3} - 1]/2$,

$$P(\rho) = B\eta\left(\frac{\rho}{\rho_0}\right)^{5/3}\left[3 + \frac{9}{2}(B' - 4)\eta + \frac{C}{9}\eta^2\right], \quad \text{(A1)}$$

with $B = 80$ GPa, $B' = 4.05$, $C = -28$. These liquid cold curve parameters were derived from extrapolation of the QMD pressure isotherms to zero temperature. It is of note that the liquid cold curve is not physically intuitive as is the solid cold curve, but it represents the underlying changes in energy and pressure due to compression alone, absent of the thermal electron and ion contributions as described by our energy decomposition of Eq. (2).

Finally for the thermal ion contribution $F_i$, a Debye model was employed in the solid phases. The Debye temperature was taken from the DFT phonon calculation as given in Table I, and a Grüneisen parameter $\gamma_{\text{ref}}$ of 2.13 was used for the fcc phase; this was primarily determined by matching the experimental thermal expansion [7]. This value was also used for the bcc phase, while the hcp phase was slightly larger at 2.25. In the liquid phase a smaller $\gamma = V(dP/dE)_V$ of 1.8 was derived from the QMD calculations by fitting the pressure energy curves and extrapolating the results to zero temperature at the ambient density of 2.71 g/cm$^3$. The model of Johnson, in particular version 2 from Ref. [29], was then found to reproduce the QMD isotherm data well, with a small energy shift relative to that of the fcc phase that then correctly determined the melt temperature at 930 K and ambient pressure. Here we use Johnson's suggested value for $a = 1.25/M^{5/3} = \theta^2/T_m\rho^{2/3}$, which relates the Debye $\theta$ and melt $T_M$, temperatures in eV along with the density $\rho$, in g/cm$^3$, where $M = 26.9815$ is the atomic mass. Additionally we make use of a model for $\gamma$ to second order in $\rho$,

$$\gamma(\rho \geqslant \rho_0) = \gamma_\infty + \frac{\rho_0}{\rho}(2\gamma_{\text{ref}} - 2\gamma_\infty + \gamma_R') + \left(\frac{\rho_0}{\rho}\right)^2(\gamma_\infty - \gamma_{\text{ref}} - \gamma_R'), \quad \text{(A2)}$$

$$\gamma(\rho < \rho_0) = \gamma_0 + \frac{\rho}{\rho_0}(2\gamma_{\text{ref}} - 2\gamma_0 - \gamma_L') + \left(\frac{\rho}{\rho_0}\right)^2(\gamma_0 - \gamma_{\text{ref}} + \gamma_L'). \quad \text{(A3)}$$

TABLE II. Parameters from the EOS for aluminum 1100.

| | $\rho$ (g/cm$^3$) | $B$ (GPa) | $B'$ | $\theta_D$ (K) |
|---|---|---|---|---|
| fcc | 2.773 | 81 | 4.70 | 385 |
| hcp | 2.749 | 76 | 4.73 | 367 |
| bcc | 2.707 | 71 | 4.69 | 355 |

Here $\gamma_{\rm ref}$ are the numbers quoted above, while $\gamma_0 = 1$ and $\gamma_\infty = 2/3$ are the values at $\rho = 0$ and $\rho = \infty$. $\gamma_L'$ and $\gamma_R'$ are the left and right logarithmic density derivatives of $\gamma$ at $\rho_0$. Both are equal to $-3$ for all the solid phases and to $-2.5$ for the liquid. Finally, there is an input of the initial melt temperature and density, which we take at 650 K and 2.48 g/cm$^3$, both below the actual melt condition. This choice provides the best agreement with the QMD and shock Hugoniot data. It does produce a melt curve within the full Johnson model that lies lower in temperature than our melt curve, which is determined by comparison of Gibbs free energies of the separately constructed phases.


[1] R. W. Lemke, D. H. Dolan, D. G. Dalton, J. L. Brown, K. Tomlinson, G. R. Robertson, M. D. Knudson, E. Harding, A. E. Mattsson, J. H. Carpenter, R. R. Drake, K. Cochrane, B. E. Blue, A. C. Robinson, and T. R. Mattsson, J. Appl. Phys. **119**, 015904 (2016).

[2] L. B. Fletcher, H. J. Lee, T. Döppner, E. Galtier, B. Nagler, P. Heimann, C. Fortmann, S. LePape, T. Ma, M. Millot, A. Pak, D. Turnbull, D. A. Chapman, D. O. Gericke, J. Vorberger, T. White, G. Gregori, M. Wei, B. Barbrel, R. W. Falcone, C.-C. Kao, H. Nuhn, J. Welch, U. Zastrau, P. Neumayer, J. B. Hastings, and S. H. Glenzer, Nat. Photon. **9**, 274 (2015).

[3] T. Ma, T. Döppner, R. W. Falcone, L. Fletcher, C. Fortmann, D. O. Gericke, O. L. Landen, H. J. Lee, A. Pak, J. Vorberger, K. Wünsch, and S. H. Glenzer, Phys. Rev. Lett. **110**, 065001 (2013).

[4] *Frontiers and Challenges in Warm Dense Matter*, Series: Lecture Notes in Computational Science and Engineering, 96, edited by F. Graziani, M. P. Desjarlais, R. Redmer, and S. B. Trickey (Springer, New York, 2014).

[5] *LASL Shock Hugoniot Data*, edited by S. P. Marsh (University of California Press, Berkeley, 1980).

[6] G. I. Kerley, Int. J. Impact Eng. **5**, 441 (1987).

[7] E. D. Chisolm, S. D. Crockett, and D. C. Wallace, Phys. Rev. B **68**, 104103 (2003).

[8] I. V. Lomonosov, Laser Part. Beams **25**, 567 (2007).

[9] L. Caillabet, S. Mazevet, and P. Loubeyre, Phys. Rev. B **83**, 094101 (2011).

[10] L. X. Benedict, K. P. Driver, S. Hamel, B. Militzer, T. Qi, A. A. Correa, A. Saul, and E. Schwegler, Phys. Rev. B **89**, 224109 (2014).

[11] S. X. Hu, L. A. Collins, V. N. Goncharov, J. D. Kress, R. L. McCrory, and S. Skupsky, Phys. Rev. E **92**, 043104 (2015).

[12] G. Kresse and J. Furthmüller, Phys. Rev. B **54**, 11169 (1996).

[13] J. P. Perdew, K. Burke, and M. Ernzerhof, Phys. Rev. Lett. **77**, 3865 (1996).

[14] G. Kresse and D. Joubert, Phys. Rev. B **59**, 1758 (1999).

[15] V. N. Staroverov, G. E. Scuseria, J. Tao, and J. P. Perdew, Phys. Rev. B **69**, 075102 (2004).

[16] P. E. Blöchl and O. Jepsen and O. K. Andersen, Phys. Rev. B **49**, 16223 (1994).

[17] M. J. Tambe, N. Bonini, and N. Marzari, Phys. Rev. B **77**, 172102 (2008).

[18] J. C. Boettger and S. B. Trickey, Phys. Rev. B **53**, 3007 (1996).

[19] K. Kunc and R. M. Martin, Phys. Rev. Lett. **48**, 406 (1982).

[20] H. R. Schober and P. H. Dederichs, in *Phonon States of Elements. Electron States and Fermi Surfaces of Alloys* edited by K.-H. Hellwege and J. L. Olsen (Springer-Verlag, Berlin, Heidelberg, 1981).

[21] Yu. B. Kudasova, O. M. Surdin, A. S. Korshunov, V. N. Pavlov, N. V. Frolova, and R. S. Kuzin, J. Exp. Theor. Phys. **117**, 664 (2013).

[22] R. G. Parr and W. Yang, *Density-Functional Theory of Atoms and Molecules* (Oxford, New York, 1989), see Chap. 9.

[23] F. Lambert, J. Clèrouin, and G. Zèrah, Phys. Rev. E **73**, 016403 (2006).

[24] T. Sjostrom and S. Crockett, Phys. Rev. B **92**, 115104 (2015).

[25] T. Sjostrom and J. Daligault, Phys. Rev. Lett. **113**, 155006 (2014).

[26] P. Giannozzi *et al.*, J. Phys.: Condens. Matter **21**, 395502 (2009).

[27] P. E. Blöchl, Phys. Rev. B **50**, 17953 (1994).

[28] E. D. Chisolm, C. W. Greeff, and D. C. George, Tech. Rep. LA-UR-05-9413, Los Alamos National Laboratory (2005).

[29] J. D. Johnson, High Press. Res. **6**, 277 (1991).

[30] C. J. Pickard and R. J. Needs, Nat. Mater. **9**, 624 (2010).

[31] V. Arp, J. H. Wilson, L. Winrich, and P. Sikora, Cryogenics **2**, 230 (1962).

[32] L. A. Willey and W. L. Fink, Trans. Am. Inst. Min., Metall. Pet. Eng. **162**, 642 (1945).

[33] M. J. Assael, K. Kakosimos, R. M. Banish, J. Brillo, I. Egry, R. Brooks, P. N. Quested, K. C. Mills, A. Nagashima, Y. Sato, and W. A. Wakeham, J. Phys. Chem. Ref. Data **35**, 285 (2006).

[34] P. M. Smith, J. W. Elmer, and G. F. Gallegos, Scr. Mater. **40**, 937 (1999).

[35] S. A. Yatsenko, V. I. Kononenko, and A. L. Sukhman, High Temp. **10**, 55 (1972).

[36] E. S. Levin, G. D. Ayushina, and P. V. Geld, High Temp. **6**, 416418 (1968).

[37] W. J. Coy and R. S. Mateer, Trans. Am. Soc. Met. **58**, 99 (1955).

[38] E. Gebhardt, M. Becker, and S. Dorner, Aluminium **31**, 315 (1955).

[39] G. Simmons and H. Wang, *Single Crystal Elastic Constants and Calculated Aggregate Properties. A Handbook 2nd Edition* (The MIT Press, Cambridge, 2009).

[40] J. C. Lashley (private communication).

[41] E. D. Eastman, A. M. Williams, and T. F. Young, J. Am. Chem. Soc. **46**, 1178 (1924).

[42] G. M. Schmiedeshoff, A. W. Lounsbury, D. J. Luna, S. J. Tracy, A. J. Schramm, S. W. Tozer, V. F. Correa, S. T. Hannahs, T. P. Murphy, E. C. Palm, A. H. Lacerda, S. L. Budko, P. C. Canfield, J. L. Smith, J. C. Lashley, and J. C. Cooley, Rev. Sci. Instrum. **77**, 123907 (2006).

[43] A. C. Mitchell and W. J. Nellis, J. Appl. Phys. **52**, 3363 (1981).

[44] L. V. Al'tshuler, S. B. Kormer, M. I. Brazhnik, L. A. Vladimirov, M. P. Speranskaya, and A. I. Funtikov, Zh. Eksp. Teor. Fiz. **38**, 1061 (1960).

[45] T. Neal, J. Appl. Phys. **46**, 2521 (1975).

[46] R. G. McQueen, J. N. Fritz, and C. E. Morris, in *Shock Waves in Condensed Matter - 83* edited by J. R. Asay, R. A. Graham, and G. K. Straub (North Holland, Amsterdam, 1984), pp. 95–98.

[47] A. Hänström and P. Lazor, J. Alloys Compd. **305**, 209 (2000).

[48] D. Errandonea, J. Appl. Phys. **108**, 033517 (2010).

[49] J. Bouchet, F. Bottin, G. Jomard, and G. Zérah, Phys. Rev. B **80**, 094102 (2009).
[50] G. I. Kerley, Kerley Technical Services Research Report KTS06-1 (2006), available at arXiv:1306.6916.
[51] L. Vočadlo and D. Alfè, Phys. Rev. B **65**, 214105 (2002).
[52] J. W. Shaner, J. M. Brown, and R. G. McQueen, *High Pressure in Science and Technology* (North Holland, Amsterdam, 1984).
[53] G. Robert, P. Legrand, P. Arnault, N. Desbiens, and J. Clérouin, Phys. Rev. E **91**, 033310 (2015).
[54] L. V. Al'tshuler, S. B. Kormer, A. A. Bakanova, and R. F. Trunin, Sov. Phys. JETP **11**, 573 (1960).
[55] L. V. Al'tshuler, S. B. Kormer, M. I. Brazhnik, L. A. Vladimirov, M. P. Speranskaya, and A. I. Funtikov, Sov. Phys. JETP **11**, 766 (1960).
[56] S. B. Kormer, A. I. Funtikov, V. D. Urlin, and A. N. Kolesnikova, Sov. Phys. JETP **15**, 477 (1962).
[57] I. C. Skidmore and E. Morris, Experimental equation-of-state data for uranium and its interpretation in the critical region, Thermodynamics of Nuclear Materials (IAEA, Vienna, 1962), p. 173.
[58] W. H. Isbell, F. H. Shipman, and A. H. Jones, Mat.Sci.Lab. Report MSL-68-13 (1968).
[59] R. G. McQueen, S. P. Marsh, J. W. Taylor, J. N. Fritz, and W. J. Carter, in *High Velocity Impact Phenomena*, edited by R. Kinslow (Academic Press, New-York, 1970), pp. 293–417, Appendices on pp. 515–568 (1970).
[60] L. V. Al'tshuler and B. S. Chekin, in *Proceeding of the All-Union Pulsed Pressures Simposium* (VNIIFTRI, Moscow, 1974) Vol. 1, pp. 5–22 (in Russian).
[61] L. V. Al'tshuler, N. N. Kalitkin, L. V. Kuz'mina, and B. S. Chekin, Sov. Phys. JETP **45**, 167 (1977).
[62] L. V. Al'tshuler, A. A. Bakanova, I. P. Dudoladov, E. A. Dynin, R. F. Trunin, and B. S. Chekin, J. Appl. Mech. Tech. Phys. **22**, 145 (1981).
[63] L. P. Volkov, N. P. Voloshin, A. S. Vladimirov, V. N. Nogin, and V. A. Simonenko, Sov. Phys. JETP Lett. **31**, 588 (1981).
[64] C. E. Ragan, Phys. Rev. A **25**, 3360 (1982).
[65] C. E. Ragan, Phys. Rev. A **29**, 1391 (1984).
[66] V. A. Simonenko, N. P. Voloshin, A. S. Vladimirov, A. P. Nagibin, V. P. Nogin, V. A. Popov, V. A. Sal'nikov, and Yu. A. Shoidin, Sov. Phys. JETP **61**, 869 (1985).
[67] R. F. Trunin, Bull. Acad. Sci. USSR, Physics of the Solid Earth **22**, 103 (1986).
[68] B. L. Glushak, A. P. Zharkov, M. V. Zhernokletov, V. Ya. Ternovoi, A. S. Filimonov, and V. E. Fortov, Sov. Phys. JETP **69**, 739 (1989).
[69] M. A. Podurets, V. M. Ktitorov, R. F. Trunin, L. V. Popov, A. Ya. Matveev, B. V. Pechenkin, and A. G. Sevast'yanov, Teplofiz. Vys. Temp. **32**, 952 (1994) (in Russian).
[70] R. F. Trunin, N. V. Panov, and A. B. Medvedev, Pis'ma Zh. Eksp. Teor. Fiz. **62**, 572 (1995) [in Russian].
[71] R. F. Trunin, M. A. Podurets, G. V. Simakov, L. V. Popov, and A. G. Sevast'yanov, Zh. Eksp. Teor. Fiz. **108**, 851 (1995) (in Russian).
[72] R. F. Trunin, N. V. Panov, and A. B. Medvedev, Chem. Phys. **14**, 97 (1995) (in Russian).
[73] R. F. Trunin, L. F. Gudarenko, M. V. Zhernokletov, and G. V. Simakov, in Extreme State of Substance. Detonation. Shock Waves: Proc. Int. Conf. VI Kharitons Topical Scientific Readings, Sarov, RFNC-VNIIEP (2001).
[74] M. D. Knudson, R. W. Lemke, D. B. Hayes, C. A. Hall, C. Deeney, and J. R. Asay, J. Appl. Phys. **94**, 4420 (2003).
[75] K. Cochrane, M. Desjarlais, T. Haill, J. Lawrence, M. Knudson, and G. Dunham, Sand Rep. SAND2006-1739, Sandia National Laboratory (2006).
[76] Y. Wang, D. Chen, and X. Zhang, Phys. Rev. Lett. **84**, 3220 (2000).
[77] D. V. Minakov, P. R. Levashov, K. V. Khishchenko, and V. E. Fortov, J. Appl. Phys. **115**, 223512 (2014).
[78] W. J. Nellis, A. C. Mitchell, and D. A. Young, J. Appl. Phys. **93**, 304 (2003).
[79] M. D. Knudson, J. R. Asay, and C. Deeney, J. Appl. Phys. **97**, 073514 (2005).
[80] M. D. Knudson, M. P. Desjarlais, and A. Pribram-Jones, Phys. Rev. B **91**, 224105 (2015).
[81] J. Clèrouin, P. Noiret, V. N. Korobenko, and A. D. Rakhel, Phys. Rev. B **78**, 224203 (2008).
[82] G. Faussurier, C. Blancard, and P. L. Silvestrelli, Phys. Rev. B **79**, 134202 (2009).
[83] V. Mishra and S. Chaturvedi, Physica B **407**, 2533 (2012).
[84] M. P. Desjarlais, AIP Conf. Proc. **1161**, 32 (2009).
[85] J.-P. Davis, J. Appl. Phys. **99**, 103512 (2006).
[86] Y. Akahama, M. Nishimura, K. Kinoshita, H. Kawamura, and Y. Ohishi, Phys. Rev. Lett. **96**, 045505 (2006).
[87] J.-P. Davis (private communication).
[88] E. D. Chisolm, Tech. Rep. LA-UR-05-2297, Los Alamos National Laboratory (2003).
[89] G. Kerley, Tech. Rep. LA-08833-M, Los Alamos National Laboratory (1981).
[90] C. Kittel, *Introduction to Solid State Physics* (John Wiley & Sons Inc., New York, 1996).